Autoxidation of alkyd resins catalyzed by iron(II) bispidine complex: drying performance and in-depth infrared study.

Martin Křižan,[a] Jaromír Vinklárek,[b] Milan Erben,[b] Ivana Císařová[c] and Jan Honzíček,[a,*]

[a] Institute of Chemistry and Technology of Macromolecular Materials, Faculty of Chemical Technology, University of Pardubice, Studentská 573, 532 10 Pardubice, Czech Republic.

[b] Department of General and Inorganic Chemistry, Faculty of Chemical Technology, University of Pardubice, Studentská 573, 532 10 Pardubice, Czech Republic.

[c] Department of Inorganic Chemistry, Faculty of Science, Charles University in Prague, Hlavova 2030/8, 128 43 Prague 2, Czech Republic.

[*] Corresponding author. Tel: +420/46603 7229. Fax: +420/46603 7068

E-mail address: jan.honzicek@upce.cz (J. Honzíček)

Keywords: bispidine; alkyd resin; autoxidation; infrared spectroscopy; 2D correlation

Highlights:

New highly active bispidine complex is reported.

X-ray structure of title compound was determined.

Catalytic power quantified by time-resolved infrared spectroscopy.

Autoxidation process followed by 2D infrared spectroscopy.

Graphical Abstract:

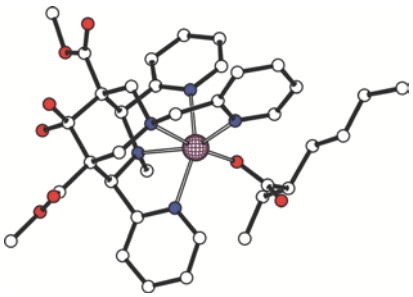

Abstract:

A new iron(II) bispidine complex with increased solubility in various organic solvents has been prepared and characterized by the spectroscopic methods and the X-ray crystallography. In depth infrared study together with

mechanical tests demonstrated the excellent catalytic performance of the iron compound in autoxidation process and established it as the potent drier suitable for solvent-borne alkyd binders. This study further reports the 2D-correlation analysis of the time-resolved infrared spectra, which was used for the first time for detailed analysis of the autoxidation process mechanism.

1. Introduction

Oxidation of polyunsaturated fatty acid tails in lipids is governed by enzymes called lipoxygenases. These non-heme iron-based enzymes, found widely in plants, fungi and animals, catalyze peroxidation of the double allylic moiety present in linoleate, linolenate and arachidonate [1]. The attempts to mimic the active site of the enzymes led to variety of non-heme iron complexes bearing polydentate ligands with nitrogen donor atoms, which catalyze oxidation reactions using hydrogen peroxide as oxidant [2-4]. In 1997, Comba *et al.* designed a new family of ligands based on the diazabicyclo[3.3.1]nonane framework (aka bispidine) [5] that bonds to iron *via* four to five nitrogen donor atoms depending on given substitution pattern [6, 7]. The very rigid ligand enforces specific geometric constrains in complexes belonging to the most powerful oxidation catalysts in the non-heme iron chemistry [8-12]. The commercially available [Fe(bispi)Cl]Cl, where bispi is dimethyl 2,4-bis(pyridin-2-yl)-3-methyl-7-(pyridin-2-ylmethyl)-3,7-diazabicyclo[3.3.1]nonan-9-one-1,5-dicarboxylate, has found an application in bleaching of textile [13]. It has been shown that this complex is also potent drier suitable for a variety of air-drying paints including alkyd binders (Scheme 1) [14], methacrylate latexes modified with fatty acids [15] and polyurethane dispersions synthesized from cardanol [16]. The quest for powerful catalysts of the autoxidation suitable for the paint producing industry is stimulated by European REACH (Registration, Evaluation, Authorisation and Restriction of Chemicals) legislation since the currently used cobalt-based driers (*e.g.* cobalt(II) 2-ethylhexanoate; **Co-Nuodex**) are under evaluation by ECHA (European Chemical Agency). In 2012, the cobalt(II) carboxylates have been classified as “CMR2–Reprotoxic” by the Cobalt REACH Consortium and may be in near future reclassified to the carcinogenic class 1B, which would restrict their use.

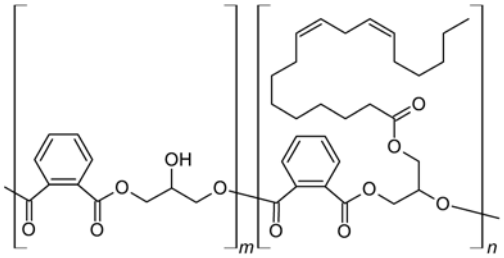

Scheme 1. Simplified structure of alkyd resin. Tail of linoleic is shown as a representative of fatty acids suitable for autoxidation drying. The ratio *m* : *n* defines the oil length of the alkyd binder [17].

Although the autoxidation of alkyd resins can be catalyzed by various manganese [18-21] and iron complexes [22, 23], most of them still suffers from some disadvantages such as a low activity at ambient temperature, an intense coloration or a low solubility in alkyd binder. Promising performance was also reported for several vanadium compounds but those are still in the early stage of the investigation [24, 25]. In fact, the cobalt(II) carboxylates could be adequately replaced still only with the manganese triazacyclononane complex [26-28] or the iron bispidine complex [Fe(bispi)Cl]Cl [28-30]. Such driers are highly active at considerably lower metal concentration than the currently used cobalt(II) carboxylates. Furthermore, the curing process, catalyzed by the cobalt-free driers, is better controlled giving a more uniform distribution of the crosslinks [31]. The main drawback of the [Fe(bispi)Cl]Cl is its low solubility in the alkyd binder and non-polar organic solvents. It is usually supplied as a solution in 1,2-propylene glycol (for solvent-borne and high-solid systems) or as an aqueous solution (for water-borne systems).

The aim of this study is to develop a new bispidine-based iron complex with increased solubility in common aprotic solvents. In present work, drying activity of the synthesized compound is tested on solvent-borne alkyd resins of different oil length (for general formula see Scheme 1). A detailed mechanism of the polymerization process is studied by *in situ* infrared spectroscopy including 2D-correlation of the time-resolved spectra.

2. Results and discussion

2.1 Synthesis and characterization of iron bispidine complex

The quest for iron complex bearing pentadentate bispidine ligand with enhanced solubility in non-polar solvents led us to a new derivative decorated with long and branched alkyl tail. Such objective has been achieved by a use of 2-ethylhexanoate that occupies the sixth position in the coordination sphere of iron. Although iron(II) 2-ethylhexanoate, necessary for synthesis of the title compound, has been reported previously [32], we decided to modify the synthetic procedure in attempt to avoid the potentially explosive inorganic perchlorate salts. Hence, our procedure uses *in-situ* neutralization of iron(II) hydroxide with 2-ethylhexanoic acid, see Scheme 2. Interestingly, the procedure is not limited to anhydrous organic solvents since the product of sufficient purity can be easily extracted from the aqueous reaction mixture by hot toluene. In the next step, the title compound, [Fe(bispi)OOCR][OOCR] (R = 3-heptyl, **Fe-bispi**), has been prepared by the reaction of the bispidine ligand with the freshly prepared iron(II) 2-ethylhexanoate, see Scheme 2.

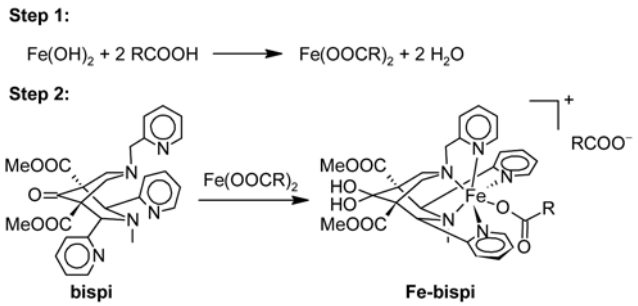

Scheme 2. Synthesis of iron(II) bispidine complex (**Fe-bispi**); R = 3-heptyl.

The **Fe-bispi** is an air-stable canary yellow solid soluble in following organic solvents: toluene, acetone, acetonitrile, methanol, organic esters and halogenoalkanes. Owing to its paramagnetic nature, **Fe-bispi** could not be satisfactorily characterized by the NMR spectroscopy. Nevertheless, the formation of the cationic species, $[Fe(bispi)OOCR]^+$, was confirmed by mass spectrometry. The compound seems to be stable in solution, as it provides a peak of the parent cation $[M]^+$. The peak assigned to $[M - H_2O]^+$ is due to water elimination from geminal diol moiety, see Scheme 2. Recrystallization of the title compound from organic solvents gives solvates with a variable composition. The well-defined solvate, **Fe-bispi**·$0.75CH_2Cl_2$, is obtained from the mixture dichloromethane – diethyl ether as confirmed by the CHN analyses and the content of iron metal (5.8 ± 0.2 wt.%) has been determined by the atomic absorption spectroscopy. Magnetic moment of the solvate (μ_{eff} = 4.85 B.M.) is very close to the spin-only value expected for the octahedral high-spin (S = 2) iron(II) species and is comparable to the data reported for similar complexes [7]. Infrared absorption bands, characteristic for the presence of ester and carboxylate groups, have been found in the region 1730–1600 cm^{-1}. Broadened bands at 2654 and 2554 cm^{-1} are due to presence of hydroxyl functions involved in strong hydrogen bond. As confirmed by the X-ray analysis of **Fe-bispi**·$0.75CH_2Cl_2$, bispi serves as pentadentate nitrogen ligand, see Figure 1. A distorted octahedral environment around the iron(II) center is completed with O1 atom of 2-ethylhexanoate anion coordinated in *trans*-position with respect to sp^3 hybridized nitrogen atom N2. The X-ray analysis further verified that the bispi ligand is ketalized to yield geminal diol upon the complexation toward iron(II) cation. Both hydroxyl groups localized at atom C4 are involved in strong hydrogen bonding toward the 2-ethylhexanoate counter ion [O7···O9 = 2.638(6) Å; O8···O10 = 2.551(6) Å].

Although the 2-ethylhexanoate anions are disordered in the crystal of the **Fe-bispi**·$0.75CH_2Cl_2$, the coordination sphere of the iron atom is well resolved (Table 1). The very rigid nature of the bispidine complex is well demonstrated on the structural parameters Fe–N and N–Fe–N, which are virtually identical to those previously reported for complexes $[Fe(bispi)Cl]Cl·H_2O$ and $[Fe(bispi)SO_4]·2MeOH$ [6].

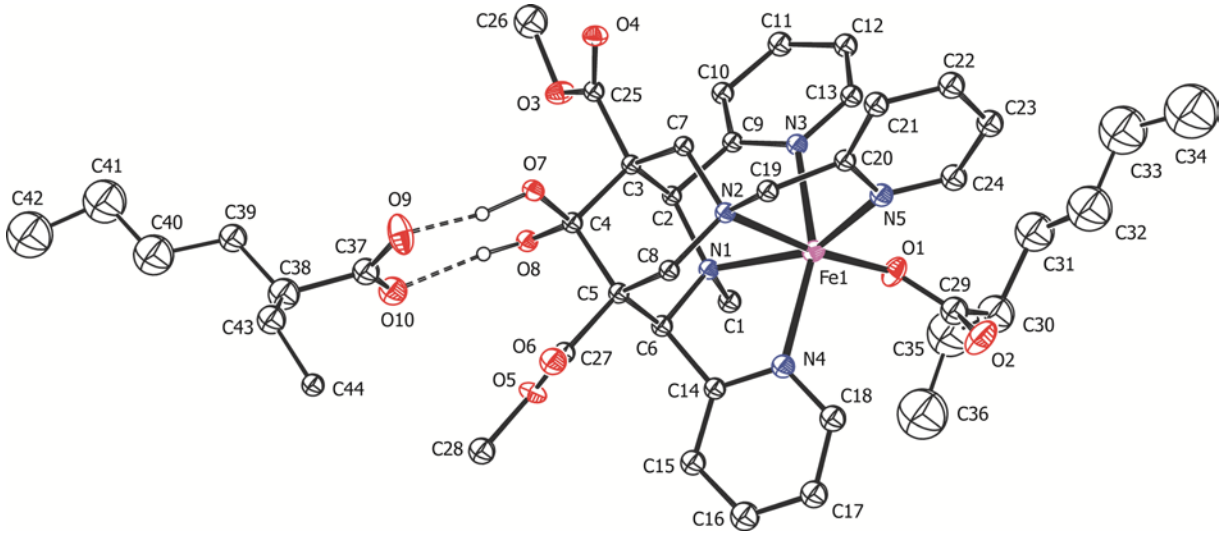

Figure 1. ORTEP drawing of iron(II) bispidine complex present in crystal structure of **Fe-bispi**·0.75CH_2Cl_2; hydrogen atoms not involved in hydrogen bonding are omitted for clarity. The labelling scheme for all non-hydrogen atoms is shown. Thermal ellipsoids are drawn at the 30% probability level.

Table 1. Selected geometric parameters describing coordination sphere of iron in **Fe-bispi**·0.75CH_2Cl_2.

Bond distances (Å)		Bond angles (°)	
Fe–O1	1.981(4)	O1–Fe–N2	173.15(14)
Fe–N1	2.195(3)	N1–Fe–N5	153.36(13)
Fe–N2	2.338(4)	N3–Fe–N4	151.99(16)
Fe–N3	2.172(5)	N1–Fe–N2	79.15(13)
Fe–N4	2.228(4)	N2–Fe–N3	88.02(15)
Fe–N5	2.158(5)	N2–Fe–N4	89.84(13)
		N2–Fe–N5	77.33(13)

*2.2 Drying performance of **Fe-bispi** in alkyd resins*

Excellent solubility of **Fe-bispi** in solvent-borne alkyd resins enables to study its drying activity in a wide range of concentrations without necessity of pre-dissolving. The performance of the complex was studied in solvent-borne phthalic-type alkyd resins of different oil length modified with soybean oil (**S40**, **S50** and **S60**). Table 2 and Tables S1 and S2 (in the Supporting Information) summarize observed drying times (τ_1 and τ_1) and relative hardness of the alkyd films ($H_{rel,5d}$ and $H_{rel,100d}$) for formulations with a different concentration of the drier. As the dry matter content of the alkyd resins was ~60%, measurements of the drying time and the relative hardness development were done on films of 76 μm and 150 μm wet thickness, respectively.

The measurements on the alkyd resin of medium oil length (**S50**) revealed excellent catalytic activity of the **Fe-bispi** at considerably lower range of metal concentrations 1×10^{-2} to 5×10^{-4} wt.% (runs **B**–**E**, see Table 2) than recommended for the commercial cobalt-based drier **Co-Nuodex** (1×10^{-1} wt.%). Hence, within this range, the alkyd coatings are dry in less than 7 h and their final relative hardness, measured 100 days after the application, varies between 44.4% and 48.9% of the glass standard. Furthermore, the fresh coatings become firm after few days of the drying as evident from the $H_{rel,5d}$ values, see Table 2.

Table 2. Drying times (τ) relative hardness (H_{rel}) and kinetic data of autoxidation process for alkyd binder **S50** treated with **Fe-bispi** (**A**–**F**) and **Co-Nuodex** (**Co-A**, **Co-B**).

Run	metal conc. (wt.%)	τ_1 [a] (h)	τ_2 [b] (h)	$H_{rel,5d}$ [c] (%)	$H_{rel,100d}$ [d] (%)	$-k_{CH,max}$ [e] (h^{-1})	t_{max} [e] (h)	IT [f] (h)	$t_{1/2}$ [g] (h)	$t_{conj.}$ [h] (h)
A	5×10^{-2}	0.8	11.5	19.2	46.8	0.70	0.2	0.1	13.1	0.3
B	1×10^{-2}	0.9	5.0	20.1	48.9	1.24	0.2	0.1	1.0	0.5
C	5×10^{-3}	0.8	4.6	19.0	46.7	0.78	0.8	0.2	1.2	1.2
D	1×10^{-3}	1.5	6.2	26.4	46.7	0.51	1.7	0.3	1.9	1.8
E	5×10^{-4}	1.5	6.5	27.1	44.4	0.32	2.7	0.6	3.2	3.9
F	1×10^{-4}	22.3	>24	n.m.	n.m.	0.02	64	–	>90	>90
Co-A [i]	1×10^{-1}	5.2	6.7	20.7 [j]	54.1	1.39	1.4	0.5	–	2.4
Co-B [i]	3×10^{-2}	19.2	24.0	22.4 [j]	49.8	0.43	13.3	10.0	–	15.8

[a] Tack free time. [b] Total dry time. [c] Relative hardness after 5 days. [d] Final relative hardness reached after 100 days. [e] Maximum autoxidation rate constant ($-k_{CH,max}$) observed at drying time t_{max}. [f] Induction time (IT) has been determined from Figure 3 graphically as intersection of horizontal line at 4.605 and tangential line extending the curve after knee point. [g] The half-life ($t_{1/2}$) is determined as point when 50% of active CH bonds are consumed. [h] The time, in which the band at 989 cm^{-1} reached maximum. [i] Data published elsewhere [25]. [j] Relative hardness after 10 days.

The optimal drying performance of the **Fe-bispi** was achieved in the run **C**, based on the very short tack-free time (τ_1 = 0.8 h) and the total dry time (τ_2 = 4.6 h). The use of lower concentrations led to gradual prolongation of the drying process. Nevertheless, the performance of the **Fe-bispi** at the lower metal concentration (run **E**) is still comparable to formulations at the optimal dosage of **Co-Nuodex** [25]. The deterioration of the catalytic activity was observed only below concentration 5×10^{-4} wt.% (run **F**) and is apparent from the long total dry times exceeding 24 h. Using iron concentrations higher than 5×10^{-3} wt.% (runs **A** and **B**), caused overdosing as

evident from longer total dry times (τ_2). At these concentrations, the autoxidation process is probably decelerated due to thin polymeric layer on the top surface of the alkyd film hindering the oxygen diffusion into the coating.

Formulations of the short-length alkyd binder **S40** are suitable for application in similar concentrations of the **Fe-bispi** as observed for the alkyd binder **S50**. In the range 1×10^{-2} to 5×10^{-4} wt.% (runs **H**–**K**, Table S1 in the Supporting Information), the tack free times are about three times longer but the total dry times are very similar not exceeding 7 hours. Final hardness of the cured films is high reaching ~50% of glass standard. Although the values are lower than observed for **Co-Nuodex** at optimal dosage (58.5%) [25], they are still sufficient for common applications [17]. Optimal dosage, estimated as the concentration when the total dry time is the shortest, was found to be 1×10^{-2} wt.% (run **H**). The first signs of overdosing were observed in the run **G** (5×10^{-2} wt.%) but even here the cured films were flat without notable visual defects.

In the case of formulations based on the long length alkyd binder **S60**, higher concentrations (1×10^{-1} to 1×10^{-3} wt.%; runs **M**–**O**; Table S2 in the Supporting Information) are necessary to get dry coating in less than 10 h. The lowest metal concentration suitable for application is comparable to the commercial **Co-Nuodex** drier [25]. The cured coatings of the formulation **Fe-bispi/S60** reach a lower final hardness ($H_{rel,100d}$ ~ 30%) than those determined for **S40** and **S50** formulations due to significantly higher content of flexible fatty acid tails in the binder molecules. Nevertheless, the values of $H_{rel,100d}$ are comparable with the **Co-Nuodex/S60** suggesting a similar density of cross-links. Interestingly, coatings dried with **Fe-bispi** become hard faster that considerably enhances their abrasion resistance during the first few days after the application. Hence, the formulations **Fe-bispi/S60** reach the relative hardness 15% after 5 days while the analogous systems dried with **Co-Nuodex** need almost a double period to get the same value of H_{rel} [25].

Effect of carboxylate ligand in coordination sphere of iron on curing activity of the drier seems to be rater small as evidenced from drying times observed for commercial [Fe(bispi)Cl]Cl (solution in 1,2-propylene glycol), see Table S3 in the Supporting Information. We note that formulations of [Fe(bispi)Cl]Cl with high metal concentration (5×10^{-2} to 5×10^{-3} wt.%) are not fully homogenous due to partial miscibility of alkyd resins with 1,2-propylene glycol. At concentration 5×10^{-2} wt.%, high concentration of the solvent results in opaque coating. Transparent film without visual defects were obtained in concentration range 1×10^{-2} to 1×10^{-4} wt.%.

2.3 In situ FTIR spectroscopy

Time-resolved FTIR spectroscopy was used for the monitoring of the autoxidation process. The assignment of interesting bands is given in Table 3. The main attention was given to the symmetrical CH stretching band of the *cis*-CH=CH moiety at 3008 cm^{-1}, whose disappearance is routinely used as a tool for determination of the rate of the autoxidation process [23, 33, 34]. Hence, its integrated area well correlates with concentration of the reactive moiety bearing isolated double bonds (see RH in Scheme 3) that rearranges during the autoxidation to the conjugated double bond system (see ROOH in Scheme 2) [35]. Time development of the band intensity in the alkyd binder **S50** at different concentration of the **Fe-bispi** is shown in Figure 2. The rapid decrease of the band intensity was observed for the runs **B**–**E**. Hence, half of the isolated *cis*-double bonds is consumed after few hours, which well correlates with short drying times given in the Table 2. At higher concentrations, the overdosing causes a rapid decrease of the reaction rate and consumption of the RH is decelerated (run **A**).

Table 3. The assignment of the FTIR bands for alkyds **S40**, **S50** and **S60**.

Wavenumber (cm^{-1})	Vibration mode
3520	ν(*O–H*) isolated [36]
3410	ν(O–*O–H*) [33]
3300 very broad	ν(*O–H*) H-bonded [36]
3008	ν_s(*cis*-C=*C–H*) [33, 37]
2926	ν_{as}(–CH_2–) [36]
2854	ν_s(–CH_2–) [36]
1708	ν(*C=O*) of saturated aldehyde [36]
1690	ν(*C=O*) of unsaturated aldehyde [36]
989	*cis-trans* conjugated C=*C–H* wagging [37]
973	isolated *trans*-C=*C–H* wagging [37]
712	(*cis*-C=*C–H*) planar bending and skeletal vibration of –$(CH_2)_n$– chain [37]

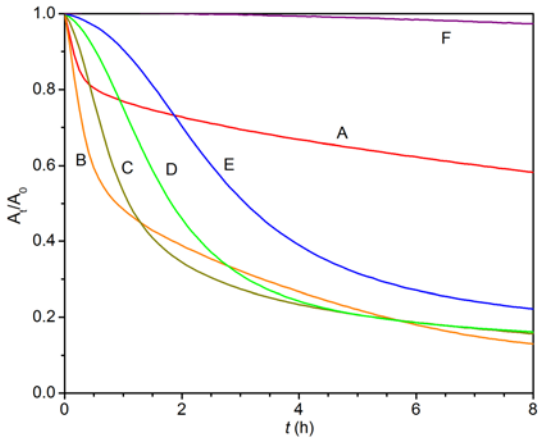

Figure 2. Time dependent integral plots of the band at 3008 cm^{-1} [ν_s(*cis*-C=*C*–*H*)] in formulation **Fe-bispi/S50**. Metal concentrations used for the runs **A**–**F** are listed in Table 2.

Based on previous kinetic experiments performed on ethyl linoleate, the hydrogen abstraction from the double allylic moiety could be taken as a pseudo-first order reaction [34]. However, such approximation can be used only for liquid system saturated with the air oxygen. In the case of alkyd binders, these conditions are fulfilled only at conversions lower than 50% ($t \leq t_{1/2}$) that is usually the point when the system solidifies and diffusion of oxygen starts to be the rate determining process.

For the runs **C**–**E**, the time dependence in the logarithmic scale is almost linear with a very short induction time (IT = 0.2–0.6 h), see Figure 3. In accordance with the obtained drying times (τ), the increase in iron concentration led to the rise of the rate coefficients and shortening of the induction time. At the higher metal concentration (run **B**), where the first signs of overdosing were evidenced by the mechanical tests, a deviation from linearity is apparent already at ~40% conversion (Figure 3). Although this formulation gives the highest rate coefficient ($-k_{CH,max}$ = 1.24 h^{-1}), the alkyd autoxidation is less effective as the uptake of oxygen is faster than its diffusion into the layer even at low conversion of the RH. Further increase of the metal concentration (run **A**) results in lower rate coefficient ($-k_{CH,max}$ = 0.70 h^{-1}) and deceleration of the catalytic process already at ~20% conversion. The autoxidation is probably too fast, producing thin skin on the top surface that considerably decelerates the oxygen diffusion.

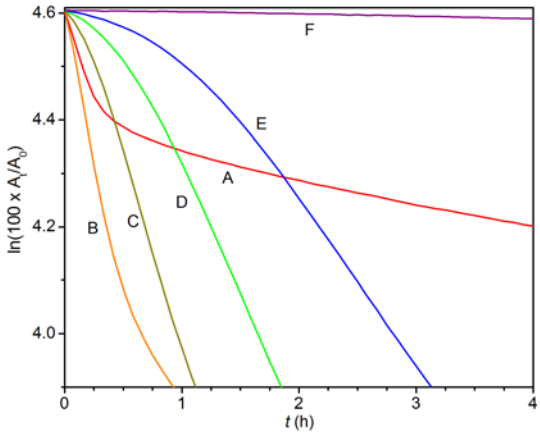

Figure 3. Region of linearity in logarithmic plots shown in Figure 2. Formulation: **Fe-bispi/S50**. Metal concentrations used for the runs **A**–**F** are listed in Table 2.

Herein applied approach describes only the beginning of the autoxidation process and, of course, cannot fully cover its complex mechanism. Nevertheless, it well correlates with the overall drying performance of the **Fe-bispi**. It is because **Fe-bispi**, similarly as many other alkyd driers, does not catalyze the direct oxidation of RH to ROOH but mainly the decomposition of ROOH already present in the commercial alkyds [14, 35]. Appearing peroxyl radicals then initiate a chain reactions producing hydroperoxides, see Scheme 3. Fast consumption of the *cis*-double bonds (RH) at the beginning of the autoxidation, therefore, implies that the reversible redox-system Fe^{II}/Fe^{III} is powerful enough to generate the radicals for both the production of ROOH and subsequent cross-linking reactions (*i.e.* the recombination and the addition of radicals to conjugated double bond systems).

Although the crosslinks formed upon the recombination of radicals are hardly traceable by infrared spectroscopy, this technique enables to follow the addition of radicals to the conjugated double bond system, shown in Scheme 4.

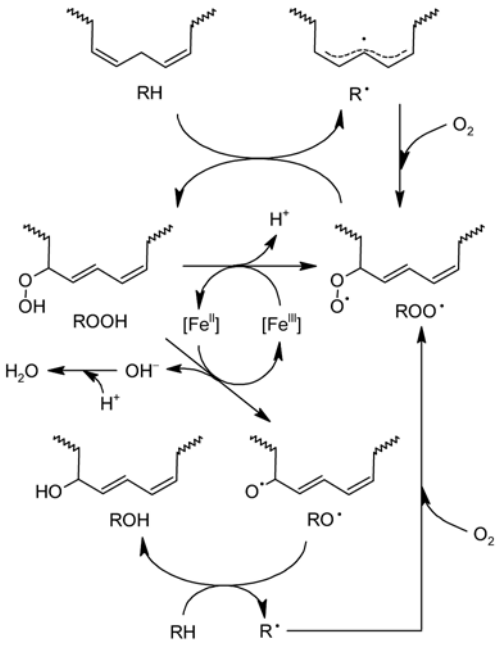

Scheme 3. Generation of radicals during the autoxidation process.

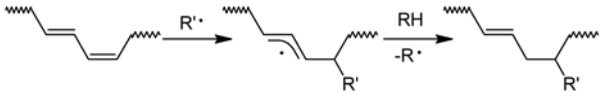

Scheme 4. Radical addition to conjugated double bond system yielding isolated *trans*-double bond. R' = R•, RO• or ROO•.

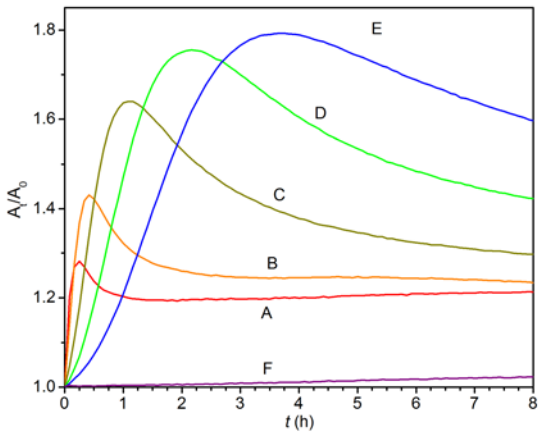

Figure 4. Time dependent plots of absorbance at 989 cm^{-1} [*cis-trans* conjugated C=*C–H* wagging]. Formulation: **Fe-bispi/S50**. Metal concentrations used for the runs **A**–**F** are listed in Table 2.

Hence, the band at 989 cm^{-1}, assigned to C–H wagging of the *cis-trans* conjugated double bond system [37], rises steeply at the beginning of the autoxidation process as the hydroperoxides are formed (see Figure 4). Their decomposition followed with simple recombination reactions yielding ROOR, ROR and RR crosslinks [38] do

not influence the band intensity since the conjugated double bond system stays untouched. Nevertheless, concentration growth of the conjugated double bonds enhances the chance for radical addition reactions. Subsequently, the appeared conjugated double bonds are consumed producing moiety with isolated *trans*-double bond, which concentration is proportional to the intensity of the band at 973 cm^{-1} (C=*C*–*H* wagging) [37]. When the radical addition prevails over the alkyd peroxidation, the intensity of the band at 989 cm^{-1} starts to decrease that becomes evident as a maximum observed on curves in the time t_{conj}, see Figure 4.

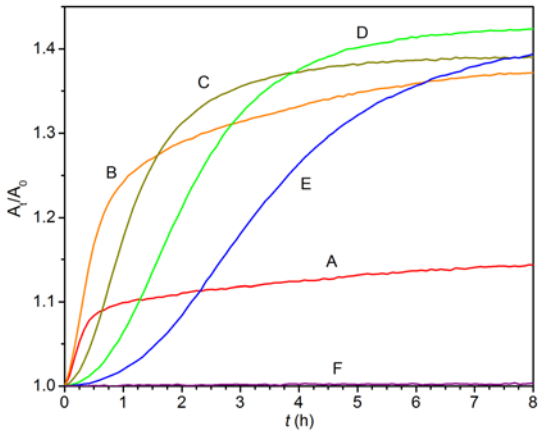

Figure 5. Time dependent plots of absorbance at 973 cm^{-1} [isolated *trans*-C=*C*–*H* wagging]. Formulation: **Fe-bispi/S50**. Metal concentrations used for the runs **A**–**F** are listed in Table 2.

As demonstrated on the alkyd binder **S50**, the higher concentrations of the drier give shorter t_{conj} (Table 2). Interestingly, the value is not influenced by overdosing that strongly contrasts with kinetic parameters related to hydroperoxide formation (*e.g.* $-k_{CH,max}$, t_{max} and $t_{1/2}$). It could be due to a slower formation of ROOH accompanied with their faster decomposition finally resulting in the significant shortening of t_{conj} in the overdosed formulations (runs **A** and **B**). Similar behavior has been observed also in the alkyd binder **S40** where the overdosing appeared at concentrations higher than 1×10^{-2} wt. % (runs **G** and **H**), see Table S1 in the Supporting Information).

The kinetic data obtained for the formulation **Fe-bispi/S60** elucidated that the relatively low efficiency of the drier, established by the mechanical test, is not a result of insufficient solubility in the alkyd binder but due to low catalytic activity in given media. The value of $-k_{CH,max}$ rises with rising metal concentration in the whole data set (runs **M**–**Q**) proving that the loss of activity is not caused by overdosing or by the presence of undissolved drier. Although the studied alkyd binders are structurally similar and contain the identical active double bond system, a higher content of the fatty acid tails in the alkyd binder **S60** dramatically lowers its

polarity. In this case, the redox system Fe^{II}/Fe^{III} is probably not enough powerful to efficiently initiate the autoxidation process.

2.4 Two-dimensional correlation analysis

To gain a more detailed insight into the performance of **Fe-bispi** in alkyd resin, the time-resolved infrared spectra were subjected to generalized two-dimensional (2D) correlation analysis. This approach enables simplification of complex spectra consisting of many overlapped peaks, enhancement of spectral resolution by spreading peaks over the second dimension and the determination of sequential order for processes related to fluctuations of given infrared bands [39, 40]. The theoretical background of 2D correlation analysis, including the summarization of possible applications, are reviewed elsewhere [41, 42]. Briefly, the cross-correlated dynamic fluctuations of infrared signals at given wavenumbers (ν_1, ν_2) produce synchronous (Φ) and asynchronous (Ψ) 2D IR spectra. The sequential order of the changes at given wavenumbers (ν_1, ν_2) can be determined from signs of the cross-peaks using following Noda's rules:

1) If $\Phi(\nu_1, \nu_2) > 0$, $\Psi(\nu_1, \nu_2) > 0$ or if $\Phi(\nu_1, \nu_2) < 0$, $\Psi(\nu_1, \nu_2) < 0$, then the movement of ν_1 is before that of ν_2 ($\nu_1 \rightarrow \nu_2$).

2) If $\Phi(\nu_1, \nu_2) > 0$, $\Psi(\nu_1, \nu_2) < 0$ or if $\Phi(\nu_1, \nu_2) < 0$, $\Psi(\nu_1, \nu_2) > 0$, then the movement of ν_1 is after that of ν_2 ($\nu_1 \leftarrow \nu_2$).

3) If $\Phi(\nu_1, \nu_2) > 0$, $\Psi(\nu_1, \nu_2) = 0$ or if $\Phi(\nu_1, \nu_2) < 0$, $\Psi(\nu_1, \nu_2) = 0$, then the movements of ν_1 and ν_2 are simultaneous ($\nu_1 \approx \nu_2$).

4) If $\Phi(\nu_1, \nu_2) = 0$, then sequential order cannot be determined.

The 2D correlation analysis of the time-resolved infrared spectra was focused mainly on a region of O–H stretching bands (3650–3100 cm^{-1}). The bands in this area originate from carboxylic functions and secondary hydroxyl groups of the alkyd backbone resulting from incomplete esterification upon the binder production. Nevertheless, our main attention was given to the hydroxyl-containing species appearing in the autoxidation process such as hydroperoxides, water and hydroxyl functions (Scheme 3). Formulation **Fe-bispi/S50** at concentration 5×10^{-4} wt.% (run **E**) was found to be very suitable for 2D analysis since the autoxidation process is slow enough for catching the most important stages. The cross-peaks appearing in the asynchronous correlation spectra, shown in Figure 6, reveal the presence of three rising bands at 3520, 3410 and 3300 cm^{-1} those could be hardly resolved by common tools because they are overlapped and broadened.

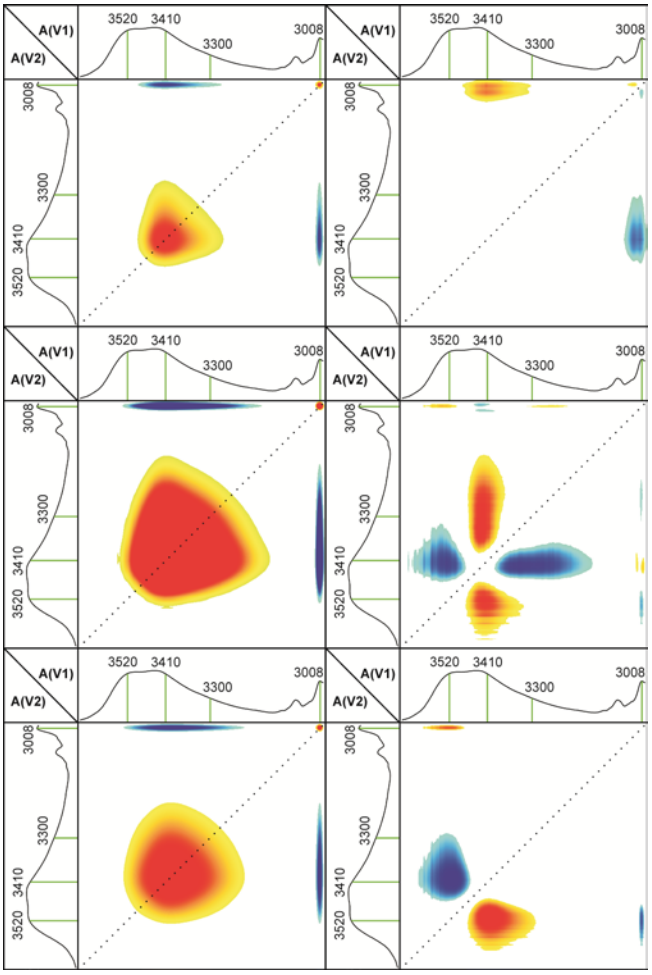

Figure 6. Synchronous (left) and asynchronous (right) correlations of the IR spectra in the region 3600–2995 cm^{-1}. Data of formulation: **Fe-bispi/S50** at metal concentration 5×10^{-4} wt.% collected at following periods: 0–50 min (first row), 50–150 min (second row) and 150–300 min (third row). Red and blue areas represent positive and negative correlation intensity, respectively.

In order to establish the detailed sequence order of consecutive reactions in the autoxidation process, the analyzed time scale has been divided into three periods. The 2D analysis of the spectra collected within the first 50 minutes reveals growth of the band at 3410 cm^{-1} that was assigned to O–H stretching of hydroperoxide function [33]. This band strongly correlates with CH stretching of the *cis*-CH=CH moiety (3008 cm^{-1}). As the corresponding synchronous and asynchronous cross-peaks are opposite in sign, the application of Noda's rules imply that the rise of band at 3410 cm^{-1} proceeds after the decrease of the band at 3008 cm^{-1} (3410 ← 3008). Such observation indicates that the autoxidation process is initiated by the catalytic decomposition of hydroperoxides already present in the alkyd binder; see Scheme 3. The initiation of radical chain reaction producing ROOH from RH is related to consumption of ROOH at early stage of autoxidation process evident from slower development of the band at 3410 cm^{-1}. The analysis of the second period (t = 50–150 min.) shows

the appearance of water and alcohols those are the main byproducts of hydroperoxide decomposition. The OH stretching modes of these species give two broad absorption bands at 3520 and 3300 cm^{-1} assignable to free and hydrogen-bonded hydroxyl groups, respectively. According to cross-peaks observed in the correlation spectra, both bands rise simultaneously after the band ascribed to ROOH:

$\Phi(3520, 3300) > 0$, $\Psi(3520, 3300) = 0$ imply (3520 ≈ 3300);

$\Phi(3410, 3520) > 0$, $\Psi(3410, 3520) > 0$ imply (3410 → 3520);

$\Phi(3410, 3300) > 0$, $\Psi(3410, 3300) > 0$ imply (3410 → 3300).

In the last period, suitable for the 2D correlation analysis (150–300 min.), the growth of the band at 3300 cm^{-1} is almost ceased suggesting the saturation of available function groups in the alkyd backbone suitable for the effective hydrogen bonding. Similarly as in the second period, the development of band ascribed to hydroperoxides precedes the band at 3520 cm^{-1} (3410 → 3520). In summary, the sequence order of the bands at 3008, 3410, 3300 and 3520 cm^{-1} can be ambiguously assigned to following consecutive conversion: RH → ROOH → H_2O + ROH. Such observation is fully in line with suggested catalytic function of **Fe-bispi** in alkyd binder, depicted in Scheme 3.

Detailed inspection of the 2D correlation spectra revealed noticeable changes in absorption bands at 2926, 2854, 1752, 1708, 1690 and 712 cm^{-1}. In accordance with previous studies, the band at 712 cm^{-1} was assigned to the in-plane bending mode of the *cis*-C=*C–H* moiety that is overlapped with the band of skeletal vibration mode of the $–(CH_2)_n–$ chain in the fatty acid tails [37]. This assignment was verified by 2D correlation analysis since the intensity of the band decreases synchronously with the consumption of active *cis*-double bonds in the course of autoxidation process [$\Phi(712, 3008) > 0$, $\Psi(712, 3008) = 0$]. The bands at 2926 and 2854 cm^{-1} were assigned to the CH stretching of methylene groups in the fatty acid tails; see Table 3. The small decrease in intensity followed with shift toward higher wavelengths, apparent from typical pattern in the asynchronous spectra (Figure 7) [43], could be ascribed to modification in close neighborhood of CH_2 groups during autoxidation resulting in the change of the extinction coefficient and energy of the vibration mode.

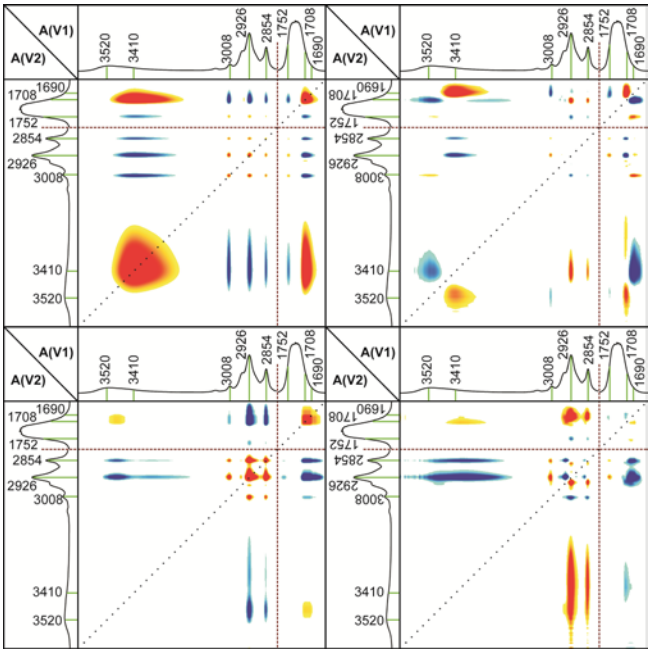

Figure 7. Synchronous (left) and asynchronous (right) correlations of the IR spectra in the regions 3650–2810 cm^{-1} and 1780–1650 cm^{-1}. Data of formulation: **Fe-bispi/S50** at metal concentration 5×10^{-3} wt.% collected at following periods: 0–100 min (first row) and 100–500 min (second row). Red and blue areas represent positive and negative correlation intensity, respectively.

The analysis of the spectra in region of C=O stretching is rather difficult due to presence of broad and very intense bands originating from ester and carboxylic groups of the polyester backbone. The small decrease of the shoulder at 1752 cm^{-1} is not fully clarified but the rise of absorbance at 1708 and 1690 cm^{-1} is attributable to the production of saturated and unsaturated aldehydes, respectively [36]. These byproducts are formed mainly by β-scission of alkoxyl radicals, see Scheme 5 [44]. The 2D correlation analysis verified that the band of unsaturated aldehyde well correlates with the band at 3520 cm^{-1} related to decay of ROOH. The application of Noda's rules further reveals different kinetic in development of the band assigned to saturated aldehydes that could be attributed to facile oxidation of these species during autoxidation process [45].

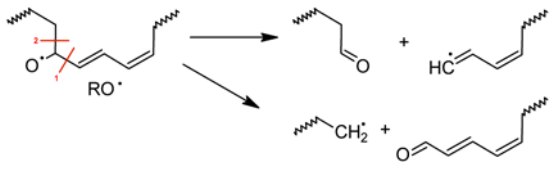

Scheme 5. Example of scission reactions giving aldehyde function groups [44].

3. Conclusion

This study described the synthesis, characterization and crystal structure of iron(II) complex bearing pentadentate bispidine ligand. Although this compound is cationic, its excellent solubility in non-polar solvents is rendered by the presence of long branched aliphatic carboxylate chains. Our experiments, performed on alkyd binders, have shown that **Fe-bispi** is a highly active autoxidation catalyst very suitable for the solvent-borne alkyd resins of short and medium oil length. Hence, it performs at about a hundred times lower metal concentration than the most widely used commercial drier **Co-Nuodex**. Furthermore, it works well at much wider range of concentrations that considerably reduces a risk of overdosing without necessity of other additives. This feature is ascribed to a different function of the complex in the mechanism of autoxidation process. Hence, the **Fe-bispi** seems to act solely as effective catalyst decomposing hydroperoxides (Scheme 3) while the cobalt-based driers have also some further functions. For example, they generate singlet oxygen, which is highly reactive toward carbon-carbon double bonds giving hydroperoxides, epoxides and endoperoxides [38]. Our in depth kinetic study, performed on the formulations dried with **Fe-bispi**, revealed that relatively low rate coefficients of the reaction RH → ROOH ($-k_{CH,max} \sim 0.3\ h^{-1}$) are necessary to reach total dry coating in few hours as common for the commercial driers. It is due to very short induction times observed even at low concentrations. Hence, this parameter was found to be a limiting factor for the cobalt compounds as demonstrated previously on the formulation **Co-Nuodex/S50**. At metal concentration 3×10^{-2} wt.%, such system reaches a comparable value of $-k_{CH,max}$ ($0.43\ h^{-1}$) but its performance is deteriorated by a long induction time (10 h) [24]. Sufficient drying activity of the **Co-Nuodex** has been obtained at concentration 1×10^{-1} wt.%, which provides considerably higher rate coefficient that is, from the kinetic point of view, the main reason for less uniform density of crosslinking (front forming drying) as the process become to be controlled by the oxygen diffusion.

The 2D-analysis of the time-resolved infrared spectra brought an in-depth insight into mechanism of autoxidation process. Such approach enabled to separate broad band of OH stretching on three absorption peaks and to assign the bands related to β-scission reactions. Nevertheless, the main outcome of the analysis is related with changes of hydroperoxide OH stretching band, whose prove that the autoxidation process is initiated with decomposition of small quantity of hydroperoxides. Although such concept is widely accepted, it is hardly observable by other experimental techniques.

In summary, the **Fe-bispi** seems to be a promising catalyst, as it accelerates the autoxidation process in the alkyd binders of short and medium oil length. In the case of binders having higher fatty acid content (*e.g.* **S60**),

the redox properties of the system Fe^{II}/Fe^{III} should be tuned in order to reach a higher efficiency in the less polar binders.

4. Experimental section

4.1 Materials

Starting bispidine ligand (bispi) was prepared following methods described elsewhere [6]. All preparative reactions were carried out under inert atmosphere of argon on a Schlenk line. All solvents used were dried and deoxygenated with appropriate drying agents, distilled under argon and degassed before use. The 2-ethylhexanoic acid (>99%, Sigma-Aldrich) was degassed and stored under argon. Cobalt(II) 2-ethylhexanoate (65 wt.% in mineral spirits, Sigma-Aldrich) and Borchi OXY-Coat ([Fe(bispi)Cl]Cl, 1 wt.% in 1,2-propylene glycol, Borchers) were used as supplied. Following solvent-borne phthalic-type alkyd resins, supplied by Spolchemie a.s., were used for both kinetic measurements and the determination of prepared films properties: alkyds modified with soybean oil CHS-Alkyd S401X55 (**S40**; oil length = 40 wt.%, dry matter = 55 wt.%, AN = 7 mg KOH/g), CHS-Alkyd S471X60 (**S50**; oil length = 47 wt.%, dry matter = 60 wt.%, AN = 6 mg KOH/g) and CHS-Alkyd S 621 W 60 (**S60**; oil length = 62 wt.%, dry matter = 60 wt.%, AN = 7 mg KOH/g). Metal concentrations are given in wt.% based on dry matter of alkyd resin.

4.2 Synthesis of iron(II) 2-ethylhexanoate

3.28 g (11.8 mmol) of $FeSO_4 \cdot 7H_2O$ was dissolved in deoxygenated water and the solution of KOH (1.32 g, 23.5 mmol in 10 ml of water) was added at once. After 10 min., the 2-ethylhexanoic acid (3.37 g, 23.4 mmol) has been added dropwise and vigorous stirring continued overnight. Resulting emulsion was extracted with hot toluene (4 × 20 ml), organic layers were decanted, combined and dried with anhydrous Mg_2SO_4. After filtration, the solvent was removed in vacuum leaving dark brown crystalline solid. Yield: 1.60 g (4.67 mmol, 40%). Analytical and spectroscopic data are in line with those published elsewhere [32].

*4.3 Synthesis of **Fe-bispi***

The suspension of finely powdered bispi (1.55 g, 3.00 mmol) in acetonitrile (50 ml) was transferred onto solid iron(II) 2-ethylhexanoate (1.54 g, 4.50 mmol). The mixture was stirred at ambient temperature until all starting materials were dissolved to give canary colored solution. Volatiles were evaporated after filtration; residue was washed with diethyl ether (3 × 10 ml) and vacuum dried. Crystallization from CH_2Cl_2/diethyl ether mixture

gives pure **Fe-bispi**·0.75CH_2Cl_2. Yield: 1.65 g (1.76 mmol, yield 59 %). Mp. 150°C (dec). Anal. Calcd. for ($C_{44}H_{61}FeN_5O_{10}$·0.75CH_2Cl_2): C, 57.21; H, 6.71; N, 7.45. Found: C, 56.84; H, 6.53; N, 7.10. The content of iron metal (5.8 ± 0.2) has been determined by atomic absorption spectroscopy. Positive-ion MS (MeCN): *m*/*z* = 714 (100%) $[M - H_2O]^+$, 732 $[M]^+$. IR (ATR-C; cm^{-1}): 3066m (ν_{CH}, aromatic), 2955vs, 2927vs, 2871s (ν_{CH}, aliphatic), 2654w, 2554m-br (ν_{OH}, H-bonded), 1728vs, 1716vs (ν_{CO}, ester), 1615s, 1599vs (ν_{CO}, carboxylate). UV-Vis [CH_2Cl_2, λ_{max}, nm, ε, log(M^{-1}·cm^{-1})]: 430 (3.60), 332 (3.04), 260 (4.24), 235sh (3.87). μ_{eff} = 4.85 ± 0.02 B. M. (at 293 K).

4.4 Spectroscopic measurements

The IR spectrum of solid **Fe-bispi** has been obtained using ATR technique (single-bounce diamond crystal, resolution 2 cm^{-1}) on Nicolet iS50 spectrophotometer. Electronic absorption spectrum (200–1080 nm) was run on a Black-Comet C-SR-100 concave grating spectrometer.

4.5 Magnetic susceptibility

Magnetic susceptibility was measured in the solid state at room temperature on Evans susceptibility balance MSB-AUTO. Corrections due to diamagnetic contribution of ligand were applied.

4.6 Mass spectrometry

Positive-ion electrospray ionization (ESI) mass spectra were recorded on a quadruple mass spectrometer (LCMS 2010, Shimadzu, Japan). The sample was injected into the mass spectrometer with infusion mode at a constant flow rate of 10 µl/min. Electrospray ionization-mass spectrometry (ESI-MS) was used for the identification of analyzed samples.

4.7 Crystal structure determination

Single-crystals of **Fe-bispi** suitable for XRD analysis were obtained by layering of saturated dichloromethane solution with diethyl ether. Crystallographic data were collected on Bruker D8 VENTURE Kappa Duo PHOTON100 by IµS micro-focus sealed tube MoKα (λ = 0.77015 Å) at a temperature of 150(2) K. The structures were solved by direct methods (SHELXL 2014/7) [46] and refined by full matrix least squares based on F^2 (SHELXL97) [47]. The hydrogen atoms on carbon were fixed into idealized positions (riding model) and assigned temperature factors either $H_{iso}(H) = 1.2\ U_{eq}$(pivot atom) or $H_{iso}(H) = 1.5$ Ueq (pivot atom) for methyl

moiety. The 2-ethylhexanoate anions are heavily disordered. The description of disorder by several partially occupied positions of carbon chain did not lead to reasonable model; therefore, only one position for the disordered atoms was used with isotropic displacement factor. On the other hand, the coordination sphere of iron atom is well resolved. CCDC-1496494 contains the supplementary crystallographic data for this paper. These data can be obtained free of charge from The Cambridge Crystallographic Data Centre via www.ccdc.cam.ac.uk/data_request/cif.

4.8 Preparation of test coatings

50.5 mg (53.7 μmol) and 10.1 mg (10.7 μmol) **Fe-bispi** was weighted on analytical balance, treated with alkyd resin **S50** (10.0 g) and stirred vigorously for 2 min with spatula to get clear solutions of metal concentration 5×10^{-2} and 1×10^{-2} wt.%, respectively. Formulations of lower concentration were prepared by dilution. 1.00 g of given formulations was diluted with 9.00 g of **S50** and homogenized to get a formulation of ten times lower concentration. The test coatings were prepared from freshly prepared formulation by frame applicators of given slot. The overall time of sample preparation did not exceed 15 min. The formulations of **S40** and **S60** were prepared accordingly. Formulations of commercial driers were prepared by standard manner. The calculated amount of the solution was weighted on analytical balance, treated with given alkyd resin (10 g) and stirred vigorously for 2 min with spatula to get clear solutions of given metal concentration.

4.9 Film drying time

The drying performance of studied catalytic systems has been determined using a BYK Drying Time Recorder. The instrument is a straight-line recorder equipped with hemispherical ended needle (5 g weight used). The needle travels the length of the test strip under standard laboratory conditions (T = 23°C, rel. humidity 50%). Glass test strip (305 × 25 × 2 mm) was prepared by casting a film upon it (thickness was 76 μm of wet film). The trace left on the film during the drying has been used to define tack free time (τ_1) and total dry time (τ_2). During the stage 1 ($t = 0–\tau_0$), the paint flows together and starts to polymerize. It gives bold and uninterrupted line. During the stage 2 ($t = \tau_1–\tau_2$), the surface is sticky and the path is ripped. After τ_2 (stage 3) the paint is through dry and needle travels on top of the surface and no trace in the film is observable.

4.10 Determination of film hardness

Film hardness development was monitored using a Persoz type pendulum (Elcometer Pendulum Hardness Tester, UK) in conformity with ISO 1522. The method is based on registering the number of pendulum swings it takes before the amplitude of the pendulum is damped to a certain extent [48]. The more swing observed, the harder is the film. Plain glass test plate (200 × 100 × 4 mm) was coated with a 150 μm film (wet thickness) dried with the appropriate drier system and film hardness was measured within 100 days. The measured value was related to the hardness of a glass standard (limit value of the pendulum test) and expressed as relative hardness. The error in determination of surface hardness was estimated to be 0.5%.

4.11 Time-resolved infrared spectroscopy

The autoxidation of alkyd resin was followed by time-resolved FTIR on spectrophotometers Nicolet 6700 and iS50 (32 scans per spectrum with a resolution of 2 cm^{-1}) in the range of 4000–500 cm^{-1}. Mixture of alkyd resin with appropriate drier was spread on the NaCl plate using an applicator with slot width 100 μm. Sample was placed in the spectrometer and IR spectrum was recorded each 5 min at 23°C. Collected IR spectra were integrated using fixed two-point baseline in the region 3014–2997 cm^{-1} (*cis*-C=*C*–*H* stretch). Rate coefficients ($-k_{CH,max}$) at the beginning of the autoxidation process were estimated as the steepest slope of the logarithmic plot of the integrated area *vs.* time. The error in determination of $k_{CH,max}$ was less than 10 % (three independent measurements for each run). The intensity of bands at 989 and 973 cm^{-1} was determined as the height of the band at these wavenumbers using linear baseline fixed at wavenumbers 1010 and 945 cm^{-1}.

4.12 2D correlation analysis

The generalized 2D correlation spectra were generated and processed by SpectraCorr 1.1 (Thermo Fisher Scientific). The analysis was performed on sets of spectra obtained from time-resolved FTIR experiments on 100 μm layer (wet width) at metal concentration 5×10^{-4} wt.% and 50 μm layer (wet width) at metal concentration 5×10^{-3} wt.%.

Acknowledgements

This work was supported by Ministry of Education of the Czech Republic (Project No. UPA SG360011).

References

[1] A. R. Brash, J. Biol. Chem. 274 (1999) 23679-23682.
[2] G. J. P. Britovsek, J. England, A. J. P. White, Inorg. Chem. 44 (2005) 8125-8134.

[3] A. Mairata i Payeras, R. Y. N. Ho, M. Fujita, L. Que Jr., Chem. Eur. J. 10 (2004) 4944-4953.
[4] Y. Hitomi, K. Arakawa, T. Funabiki, M. Kodera, Angew. Chem. Int. Ed. 51 (2012) 3448-3452.
[5] P. Comba, B. Nuber, A. Ramlow, J. Chem. Soc., Dalton Trans. (1997) 347-352.
[6] H. Börzel, P. Comba, K. S. Hagen, Y. D. Lampeka, A. Lienke, G. Linti, M. Merz, H. Pritzkow, L. V. Tsymbal, Inorg. Chim. Acta 337 (2002) 407-419.
[7] P. Comba, H. Rudolf, H. Wadepohl, Dalton Trans. 44 (2015) 2724-2736.
[8] M. R. Bukowski, P. Comba, C. Limberg, M. Merz, L. Que Jr., T. Wistuba, Angew. Chem. Int. Ed. 43 (2004) 1283-1287.
[9] P. Comba, Y. M. Lee, W. Nam, A. Waleska, Chem. Commun. 50 (2014) 412-414.
[10] P. Comba, M. Maurer, P. Vadivelu, Inorg. Chem. 48 (2009) 10389-10396.
[11] M. R. Bukowski, P. Comba, A. Lienke, C. Limberg, C. L. de Laorden, R. Mas-Ballesté, M. Merz, L. Que Jr., Angew. Chem. Int. Ed. 45 (2006) 3446-3449.
[12] J. Bautz, P. Comba, C. L. de Laorden, M. Menzel, G. Rajaraman, Angew. Chem. Int. Ed. 46 (2007) 8067-8070.
[13] R. Hage, A. Lienke, Angew. Chem. Int. Ed. 45 (2006) 206-222.
[14] J. W. de Boer, P. V. Wesenhagen, E. C. M. Wenker, K. Maaijen, F. Gol, H. Gibbs, R. Hage, Eur. J. Inorg. Chem. (2013) 3581-3591.
[15] M. Moreno, C. Lampard, N. Williams, E. Lago, S. Emmett, M. Goikoetxea, M. J. Barandiaran, Prog. Org. Coat. 81 (2015) 101-106.
[16] C. J. Patel, V. Mannari, Prog. Org. Coat. 77 (2014) 997-1006.
[17] W. T. Elliott, in *Surface Coatings: Volume 1 Raw Materials and Their Usage*, Chapman & Hall, London, **1993**, pp. 76-109.
[18] J. Z. Wu, E. Bouwman, J. Reedijk, Prog. Org. Coat. 49 (2004) 103-108.
[19] R. van Gorkum, F. Buda, H. Kooijman, A. L. Spek, E. Bouwman, J. Reedijk, Eur. J. Inorg. Chem. (2005) 2255-2261.
[20] E. Bouwman, R. van Gorkum, J. Coat. Technol. Res. 4 (2007) 491-503.
[21] Z. O. Oyman, W. Ming, R. van der Linde, R. van Gorkum, E. Bouwman, Polymer 46 (2005) 1731-1738.
[22] F. Micciche, E. Oostveen, J. van Haveren, R. van der Linde, Prog. Org. Coat. 53 (2005) 99-105.
[23] M. Erben, D. Veselý, J. Vinklárek, J. Honzíček, J. Mol. Catal. A: Chem. 353-354 (2012) 13-21.
[24] O. Preininger, J. Vinklárek, J. Honzíček, T. Mikysek, M. Erben, Prog. Org. Coat. 88 (2015) 191-198.
[25] O. Preininger, J. Honzíček, P. Kalenda, J. Vinklárek, J. Coat. Technol. Res. 13 (2016) 479-487.
[26] Z. O. Oyman, W. Ming, R. van der Linde, Appl. Catal. A 316 (2007) 191-196.
[27] Z. O. Oyman, W. Ming, F. Micciche, E. Oostveen, J. van Haveren, R. van der Linde, Polymer 45 (2004) 7431-7436.
[28] R. Hage, J. W. de Boer, K. Maaijen, Inorganics 4 (2016) 11.
[29] B. Pirš, B. Znoj, S. Skale, J. Zabret, J. Godnjavec, P. Venturini, J. Coat. Technol. Res. 12 (2015) 965-974.
[30] B. Pirš, B. Znoj, S. Skale, J. Zabret, J. Godnjavec, P. Berce, P. Venturini, Acta Chim. Slov. 62 (2015) 52-59.
[31] Ö. Gezici-Koc, C. A. A. M. Thomas, M. E. B. Michel, S. J. F. Erich, H. P. Huinink, J. Flapper, F. L. Duivenvoorde, L. G. J. van der Ven, O. C. G. Adan, Mater. Today Commun. 7 (2016) 22-31.
[32] F. Micciche, J. van Haveren, E. Oostveen, W. Ming, R. van der Linde, Appl. Catal. A 297 (2006) 174-181.
[33] F. R. van de Voort, A. A. Ismail, J. Sedman, G. Emo, J. Am. Oil Chem. Soc. 71 (1994) 243-253.
[34] S. T. Warzeska, M. Zonneveld, R. van Gorkum, W. J. Muizebelt, E. Bouwman, J. Reedijk, Prog. Org. Coat. 44 (2002) 243-248.
[35] R. van Gorkum, E. Bouwman, Coord. Chem. Rev. 249 (2005) 1709-1728.
[36] G. Socrates, *Infrared and Raman Characteristic Group Frequencies: Tables and Charts*, 3rd ed., John Wiley & Sons, Chichester, **2004**.
[37] Z. O. Oyman, W. Ming, R. van der Linde, Prog. Org. Coat. 48 (2003) 80-91.
[38] M. D. Soucek, T. Khattab, J. Wu, Prog. Org. Coat. 73 (2012) 435-454.
[39] I. Noda, J. Am. Chem. Soc. 111 (1989) 8116-8118.
[40] C. Marcott, A. E. Dowrey, I. Noda, Anal. Chem. 66 (1994) 1065A-1075A.
[41] I. Noda, Appl. Spectrosc. 44 (1990) 550-561.
[42] Y. Ozaki, in *Handbook of Vibrational Spectroscopy*, John Wiley & Sons, **2006**, pp. 2136-2172.
[43] S. Morita, H. Shinzawa, I. Noda, Y. Ozaki, J. Mol. Struct. 799 (2006) 16-22.
[44] W. W. Nawar, J. Chem. Educ. 61 (1984) 299-302.
[45] M. Lazzari, O. Chiantore, Polym. Degrad. Stab. 65 (1999) 303-313.
[46] G. M. Sheldrick, SHELXL2014/7, University of Göttingen, Germany (2017).

[47] G. M. Sheldrick, Acta Cryst. A64 (2008) 112-122.
[48] B. Persoz, *Peintures, Pigments, Vernis* 21 (1945) 194-201.

Supporting material (for publication):

Table S1. Drying times (τ) relative hardness (H_{rel}) and kinetic data of autoxidation process for alkyd binder **S40** treated with **Fe-bispi** (**G**–**L**) and **Co-Nuodex** (**Co-C**).

Run	metal conc. (wt.%)	τ_1 [a] (h)	τ_2 [b] (h)	$H_{rel,5d}$ [c] (%)	$H_{rel,100d}$ [d] (%)	$-k_{CH,max}$ [e] (h^{-1})	t_{max} [e] (h)	IT [f] (h)	$t_{1/2}$ [g] (h)	$t_{conj.}$ [h] (h)
G	5×10^{-2}	0.8	4.2	37.2	49.8	0.80	0.2	0.1	1.9	0.6
H	1×10^{-2}	2.9	3.1	37.0	48.9	0.63	0.8	0.1	1.7	1.3
I	5×10^{-3}	3.3	3.7	34.2	47.5	0.54	1.7	0.4	2.1	2.2
J	1×10^{-3}	4.6	6.5	39.4	51.1	0.42	2.1	0.5	2.7	3.0
K	5×10^{-4}	6.2	6.9	35.2	47.4	0.21	2.6	0.6	4.1	5.3
L	1×10^{-4}	>24	>24	n.m.	n.m.	n.m.	n.m.	n.m.	n.m.	n.m.
Co-C [i]	6×10^{-2}	2.7	6.9	35.3 [j]	58.5	0.79	0.9	–	–	2.0

[a] Tack free time. [b] Total dry time. [c] Relative hardness after 5 days. [d] Final relative hardness reached after 100 days. [e] Maximum autoxidation rate constant ($k_{CH,max}$) observed at drying time t_{max}. [f] Induction time (IT) has been determined from Figure S2 graphically as intersection of horizontal line at 4.605 and tangential line extending the curve after knee point. [g] The half-life ($t_{1/2}$) is determined as point when 50% of active CH bonds are consumed. [h] The time, in which the band at 989 cm^{-1} reached maximum. [i] Data published elsewhere [25]. [j] Relative hardness after 10 days.

Table S2. Drying times (τ) relative hardness (H_{rel}) and kinetic data of autoxidation process for alkyd binder **S60** treated with **Fe-bispi** (**M**–**Q**) and **Co-Nuodex** (**Co-D**)

Run	Fe conc. (wt.%)	τ_1 [a] (h)	τ_2 [b] (h)	$H_{rel,5d}$ [c] (%)	$H_{rel,100d}$ [d] (%)	$-k_{CH,max}$ [e] (h^{-1})	t_{max} [e] (h)	IT [f] (h)	$t_{1/2}$ [g] (h)	$t_{conj.}$ [h] (h)
M	1×10^{-1}	0.8	3.9	16.7	30.2	0.49	2.0	0.8	2.4	2.5
N	5×10^{-2}	1.5	6.1	16.0	30.0	0.33	2.1	1.1	3.5	2.8
O	1×10^{-2}	5.4	8.5	15.1	28.2	0.11	8.4	4.5	11.8	13.8
P	5×10^{-3}	9.2	10.4	15.4	27.8	0.06	14	6.5	20.8	22.9
Q	1×10^{-3}	>24	>24	11.0	25.7	n.m.	n.m.	n.m.	n.m.	n.m.
Co-D [i]	1×10^{-1}	0.8	4.6	16.0 [j]	39.4	1.56	0.6	–	–	1.4

[a] Tack free time. [b] Total dry time. [c] Relative hardness after 5 days. [d] Final relative hardness reached after 100 days. [e] Maximum autoxidation rate constant ($k_{CH,max}$) observed at drying time t_{max}. [f] Induction time (IT) has been determined from Figure S7 graphically as intersection of horizontal line at 4.605 and tangential line extending the curve after knee point. [g] The half-life ($t_{1/2}$) is determined as point when 50% of active CH bonds are consumed. [h] The time, in which the band at 989 cm^{-1} reached maximum. [i] Data published elsewhere [25]. [j] Relative hardness after 10 days.

Table S3. Drying times (τ) for alkyd binders **S40**, **S50** and **S60** treated with [Fe(bispi)Cl]Cl.

Alkyd	metal conc. (wt.%)	τ_1 [a] (h)	τ_2 [b] (h)	Alkyd	metal conc. (wt.%)	τ_1 [a] (h)	τ_2 [b] (h)	Alkyd	metal conc. (wt.%)	τ_1 [a] (h)	τ_2 [b] (h)
S40	5×10^{-2}	0.7 [c]	>24 [c]	**S50**	5×10^{-2}	1.5 [c]	11.0 [c]	**S60**	5×10^{-2}	– [d]	– [d]
S40	1×10^{-2}	0.7	8.2	**S50**	1×10^{-2}	1.6	4.8	**S60**	1×10^{-2}	0.7	4.6
S40	5×10^{-3}	0.4	9.9	**S50**	5×10^{-3}	1.0	3.2	**S60**	5×10^{-3}	1.2	4.6
S40	1×10^{-3}	0.8	6.7	**S50**	1×10^{-3}	2.6	7.1	**S60**	1×10^{-3}	2.6	7.2
S40	5×10^{-4}	2.9	8.9	**S50**	5×10^{-4}	4.5	7.9	**S60**	5×10^{-4}	6.5	14.9
S40	1×10^{-4}	13.1	>24	**S50**	1×10^{-4}	12.3	>24	**S60**	1×10^{-4}	>24	>24

[a] Tack free time. [b] Total dry time. [c] Non-transparent opaque film is formed. [d] Drier separates out of the alkyd film; drying time was not estimated.

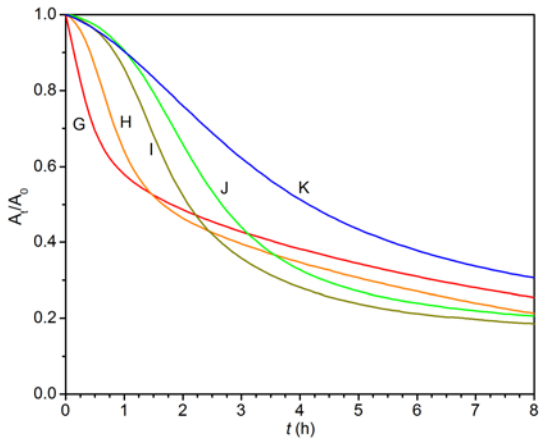

Figure S1. Time dependent integral plots of the band at 3008 cm^{-1} in formulation **Fe-bispi/S40**. Metal concentrations used for the runs **G**–**K** are listed in Table S1.

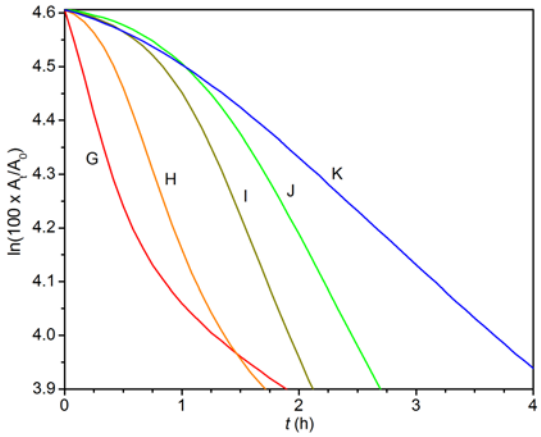

Figure S2. Time dependent integral plots of the band at 3008 cm^{-1} in logarithmic scale. Formulation: **Fe-bispi/S40**. Metal concentrations used for the runs **G**–**K** are listed in Table S1.

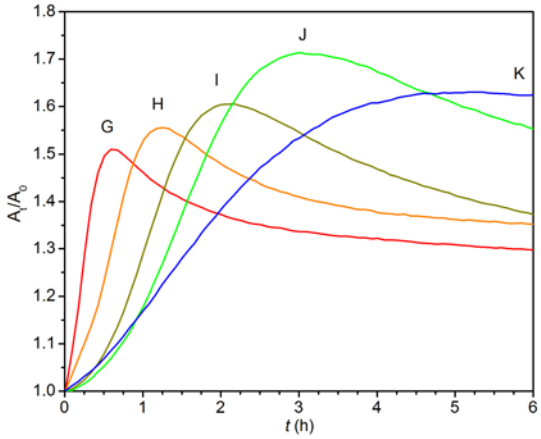

Figure S3. Time dependent plots of absorbance at 989 cm^{-1}. Formulation: **Fe-bispi/S40**. Metal concentrations used for the runs **G**–**K** are listed in Table S1.

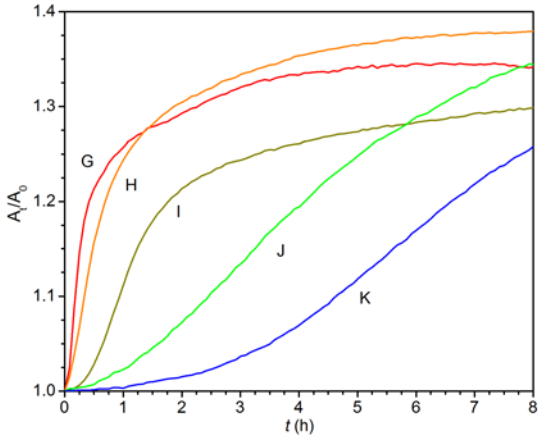

Figure S4. Time dependent plots of absorbance at 973 cm^{-1}. Metal concentrations used for the runs **G**–**K** are listed in Table S1.

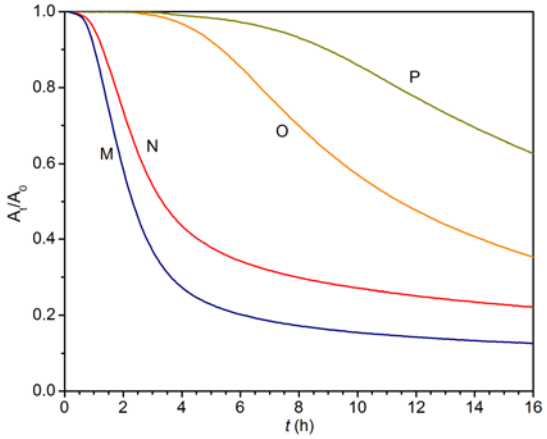

Figure S5. Time dependent integral plots of the band at 3008 cm^{-1} in formulation **Fe-bispi/S60**. Metal concentrations used for the runs M–P are listed in Table S2.

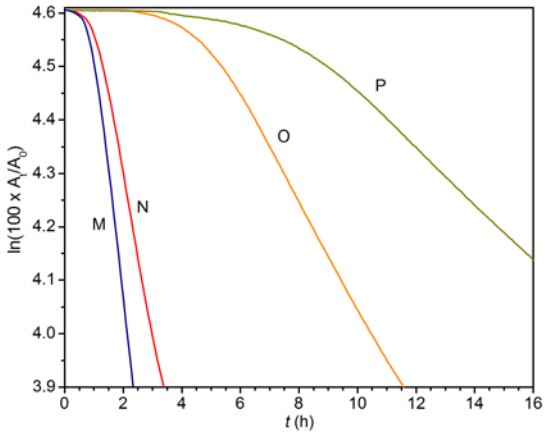

Figure S6. Time dependent integral plots of the band at 3008 cm^{-1} in logarithmic scale. Formulation: **Fe-bispi/S60**. Metal concentrations used for the runs **M**–**P** are listed in Table S2.

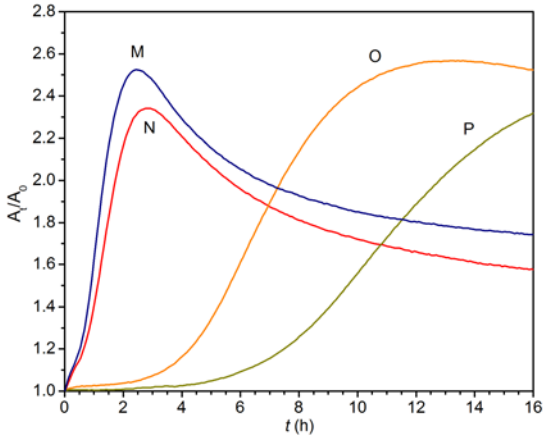

Figure S7. Time dependent plots of absorbance at 989 cm^{-1}. Formulation: **Fe-bispi/S60**. Metal concentrations used for the runs **M**–**P** are listed in Table S2.

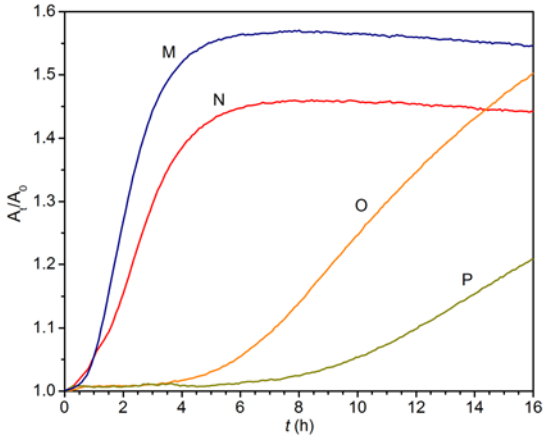

Figure S8. Time dependent plots of absorbance at 973 cm^{-1}. Formulation: **Fe-bispi/S60**. Metal concentrations used for the runs **M**–**P** are listed in Table S2.